

## Supporting Information

# Efficient Hydrogen Production via Sunlight-driven Thermal Formic Acid Decomposition over Porous Film of Molybdenum Carbide

*Cuncai Lv,<sup>a,b</sup> Pingping Lou,<sup>a</sup> Chengcheng Shi,<sup>a</sup> Ruining Wang,<sup>\*a</sup> Yanhui Fu,<sup>a</sup> Linjie Gao,<sup>a</sup> Shufang Wang,<sup>a</sup> Yaguang Li,<sup>\*a</sup> Chi Zhang<sup>\*b</sup>*

[a] Key Laboratory of High-precision Computation and Application of Quantum Field Theory of Hebei Province, Institute of Life Science and Green Development, The College of Physics Science and Technology, Hebei University, Baoding, 071002, P.R. China.

[b] School of Chemical Science and Engineering, Institute for Advanced Study, Tongji University, Shanghai, 200092, P. R. China.

\* Ruining Wang, E-mail: rnwang@hbu.edu.cn; Yaguang Li, E-mail: liyaguang@hbu.edu.cn; Chi Zhang, E-mail: [chizhang@tongji.edu.cn](mailto:chizhang@tongji.edu.cn)

Supporting discussion S1. Estimation of the **PF-Mo<sub>1.98</sub>C<sub>1.02</sub>** weight content in the composite

The PF-Mo<sub>1.98</sub>C<sub>1.02</sub> was exfoliated from the carbon fiber paper (CFP) via ultrasonic vibration, and subjected to thermogravimetric analysis (TGA). At 650 °C, all the carbon atoms (including residual carbon and those in Mo<sub>1.98</sub>C<sub>1.02</sub>) were removed, and all the Mo<sub>1.98</sub>C<sub>1.02</sub> was oxidized to MoO<sub>3</sub> during the oxidation process. The weight percent of Mo<sub>1.98</sub>C<sub>1.02</sub> in the PF-Mo<sub>1.98</sub>C<sub>1.02</sub> is computed according to the follow equation:

$$\frac{1.98W_{Mo1.98C1.02}}{M_{Mo1.98C1.02}} = \frac{W_{remain}}{M_{MoO3}}$$

Where W<sub>Mo1.98C1.02</sub> is the weight percent of Mo<sub>1.98</sub>C<sub>1.02</sub>, M<sub>Mo1.98C1.02</sub> is the molecular weight of Mo<sub>1.98</sub>C<sub>1.02</sub>, W<sub>remain</sub> is the weight of MoO<sub>3</sub> suggested by the TGA curve, M<sub>MoO3</sub> is the molecular weight of MoO<sub>3</sub>. According to the TGA curve, W<sub>remain</sub> is 121.74%, and then W<sub>Mo1.98C1.02</sub> is computed to be 86.38%. Therefore, the weight percent of residual carbon is 1 – 86.38% = 13.62%.

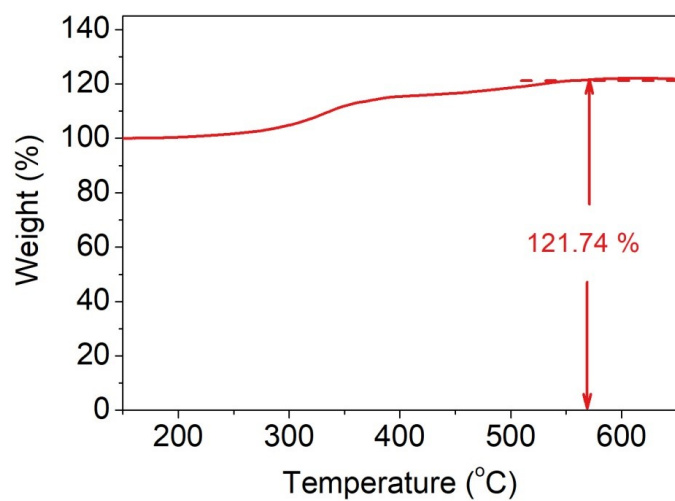


**Figure S1.** TGA curve of PF-Mo<sub>1.98</sub>C<sub>1.02</sub> measured in O<sub>2</sub> atmosphere.

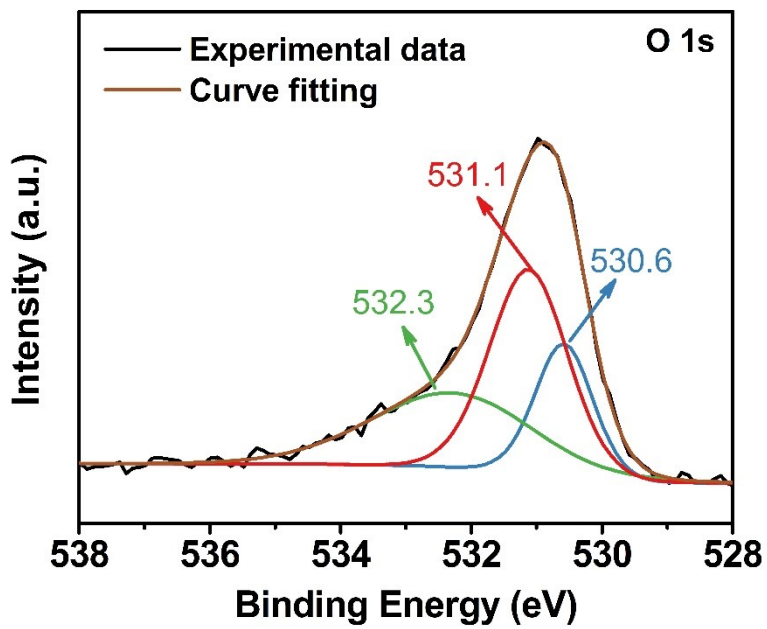


**Figure S2.** O 1s window XPS spectra of the PF-Mo<sub>1.98</sub>C<sub>1.02</sub>.

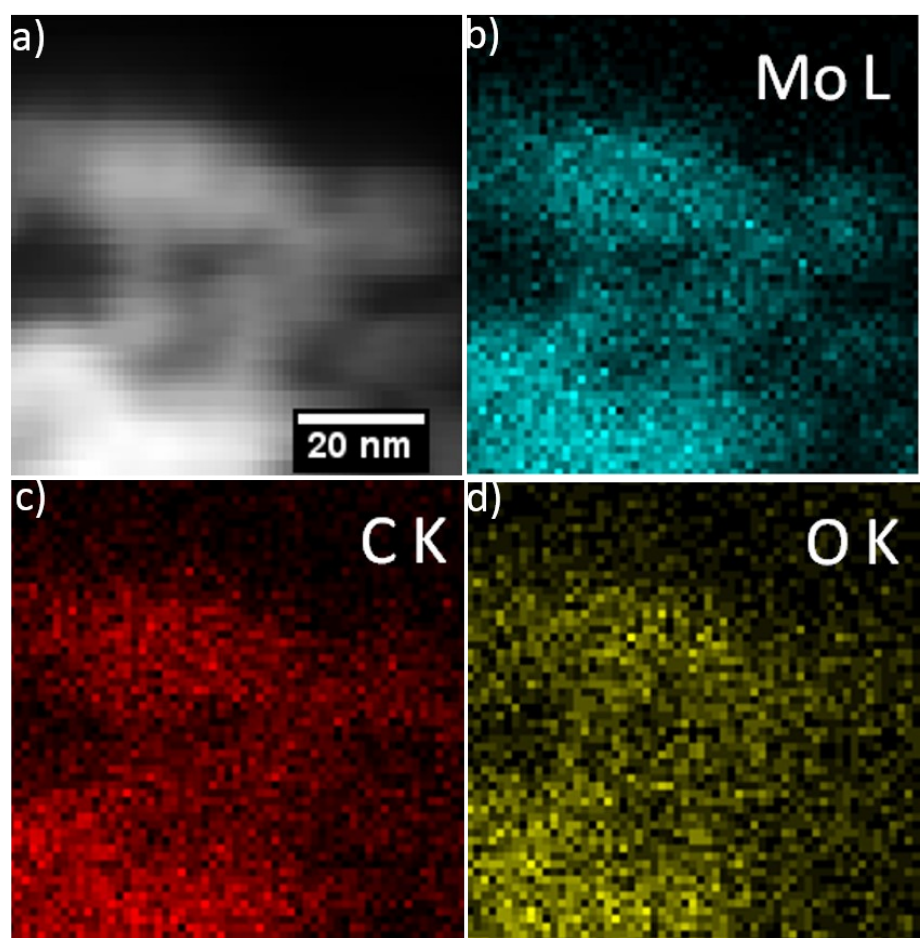


**Figure S3.** (a) Dark-field STEM image of the PF-Mo<sub>1.98</sub>C<sub>1.02</sub> and corresponding elemental mapping images of (b) Mo, (c) C, and (d) O.

**Table S1.** Performances of representative highly efficient molybdenum-based catalysts

toward the thermal catalytic FA decomposition.

Catalyst	Temperatur e (°C)	Conversion (%)	H <sub>2</sub> selectivity (%)	H <sub>2</sub> generation rate (L g <sup>-1</sup> h <sup>-1</sup> )	Reference
γ-Mo <sub>2</sub> N/NC	100	10	99.04	0.185	<sup>1</sup>
1% Mo <sub>2</sub> C/Norit	100	25	100	0.1-0.12	<sup>2</sup>
	150	100	100	0.4-0.48	
10Mo <sub>x</sub> C/AC	100	7	91	0.070	<sup>3</sup>
	200	100	92	1.012	
Mo <sub>2</sub> C/Gr	380	37	86	--	<sup>4</sup>
MoS <sub>2</sub> /Graphene	145	12	24	2.50	<sup>5</sup>
Fe-MoC <sub>1-x</sub>	100	5	100	--	<sup>6</sup>
	200	58	94	--	
Mg-MoC <sub>1-x</sub>	100	0	100	--	<sup>6</sup>
	200	94	92	--	
Soy-Mo	100	41	99.25	--	<sup>7</sup>
	120	85	99.1	--	
α-Mo <sub>x</sub> C <sub>y</sub> nanosheets	100	0	100	--	<sup>7</sup>
	300	100	89	--	
Mo <sub>2</sub> C-Co/GAC	100	56.3	99.9	0.293	<sup>8</sup>
	200	100	99.6	0.521	
PF-Mo <sub>1.98</sub> C <sub>1.02</sub>	100	--	97.6	0.79	This work

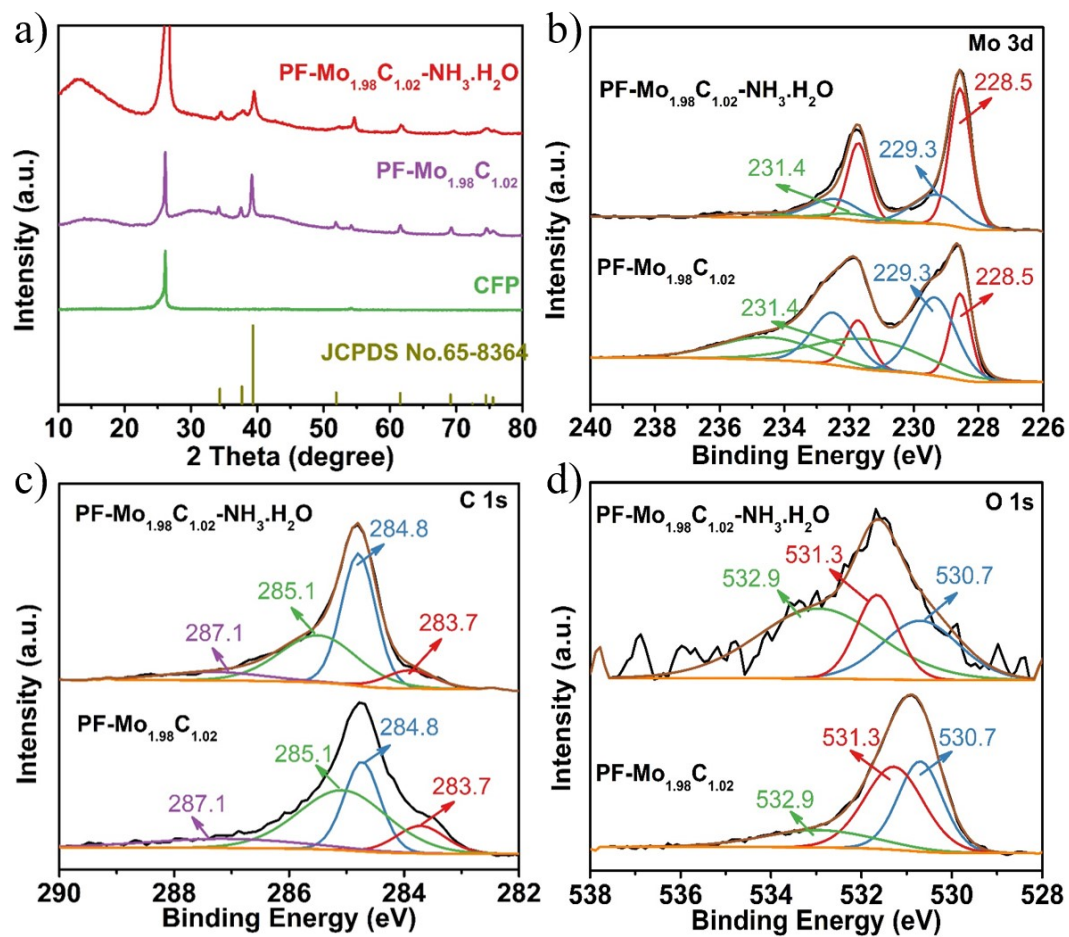


**Figure S4.** (a) XRD pattern, (b) Mo 3d window, (c) C 1s window and (d) O 1s window

XPS spectra of the PF-Mo<sub>1.98</sub>C<sub>1.02</sub> before and after NH<sub>3</sub>·H<sub>2</sub>O immersion.

**Table S2.** Fitting parameters (binding energy, peak area and species percentage) for Mo<sup>2+</sup>, Mo<sup>4+</sup> and Mo<sup>5+</sup> spectra taken on pristine PF-Mo<sub>1.98</sub>C<sub>1.02</sub>, PF-Mo<sub>1.98</sub>C<sub>1.02</sub> after FA decomposition test and PF-Mo<sub>1.98</sub>C<sub>1.02</sub> after NH<sub>3</sub>·H<sub>2</sub>O immersion.

Samples	Species		Binding energy	Peak area	Species percentage	Mo <sub>Mo-O</sub> /Mo <sub>Mo-C</sub>
PF-Mo <sub>1.98</sub> C <sub>1.02</sub>	Mo-C	Mo <sup>2+</sup>	228.5	20835	0.21	0.79/0.21
	Mo-O	Mo <sup>4+</sup>	229.3	38868	0.40	
		Mo <sup>5+</sup>	231.4	38375	0.39	
PF-Mo <sub>1.98</sub> C <sub>1.02</sub> after test	Mo-C	Mo <sup>2+</sup>	228.5	11497	0.20	0.80/0.20
	Mo-O	Mo <sup>4+</sup>	229.3	27328	0.47	
		Mo <sup>5+</sup>	231.6	19803	0.33	
PF-Mo <sub>1.98</sub> C <sub>1.02</sub> - NH <sub>3</sub> ·H <sub>2</sub> O	Mo-C	Mo <sup>2+</sup>	228.5	5078	0.63	0.37/0.63
	Mo-O	Mo <sup>4+</sup>	229.3	2439	0.30	
		Mo <sup>5+</sup>	231.4	600	0.07	

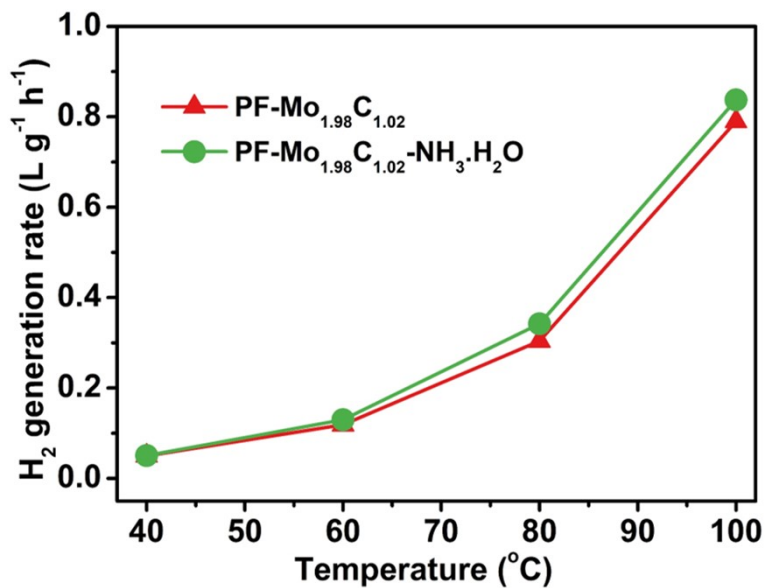


**Figure S5.** Temperature dependent H<sub>2</sub> generation rate of PF-Mo<sub>1.98</sub>C<sub>1.02</sub> and PF-Mo<sub>1.98</sub>C<sub>1.02</sub>-NH<sub>3</sub>·H<sub>2</sub>O from FA decomposition.

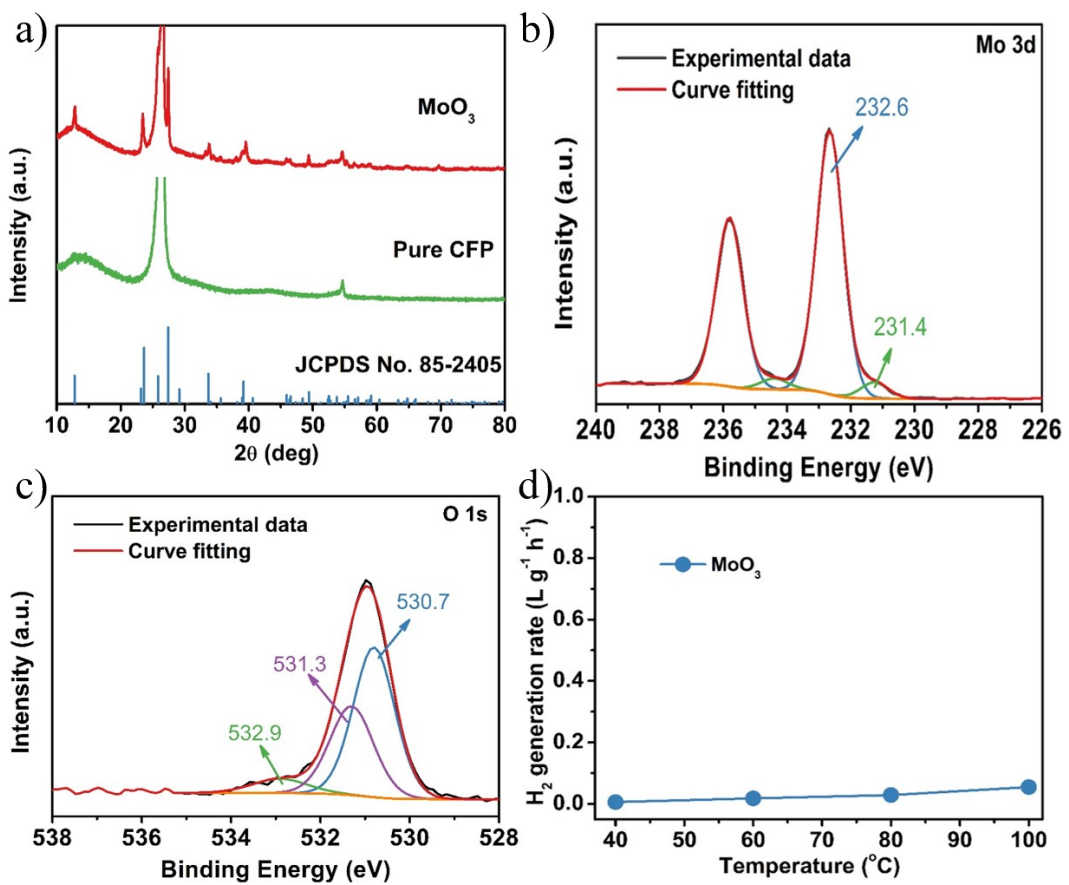


**Figure S6.** (a) XRD pattern, (b) Mo 3d window and (c) O 1s window XPS spectra of the  $\text{MoO}_3$ . (d) Temperature dependent  $\text{H}_2$  generation rate of  $\text{MoO}_3$  from FA decomposition.

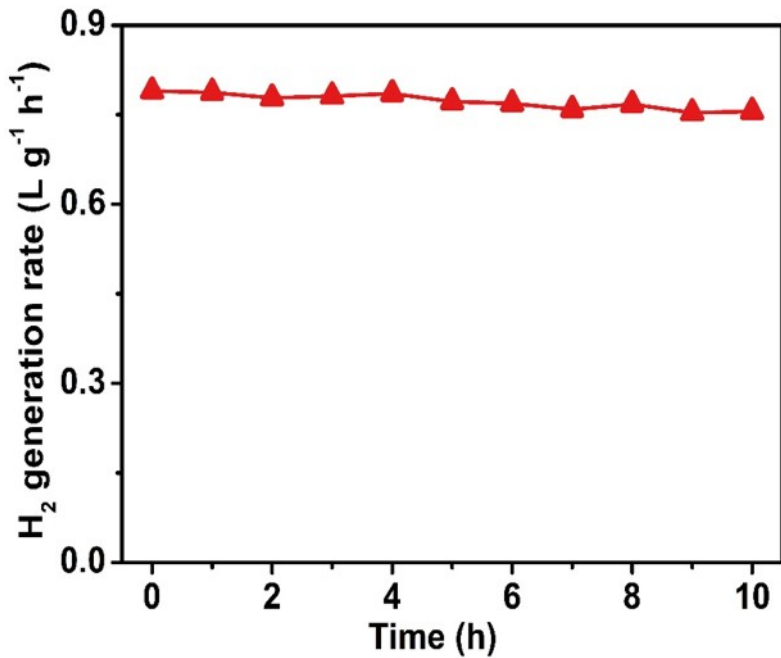


**Figure S7.** FA decomposition stability of  $\text{PF}-\text{Mo}_{1.98}\text{C}_{1.02}$  under the temperature of 100 °C.

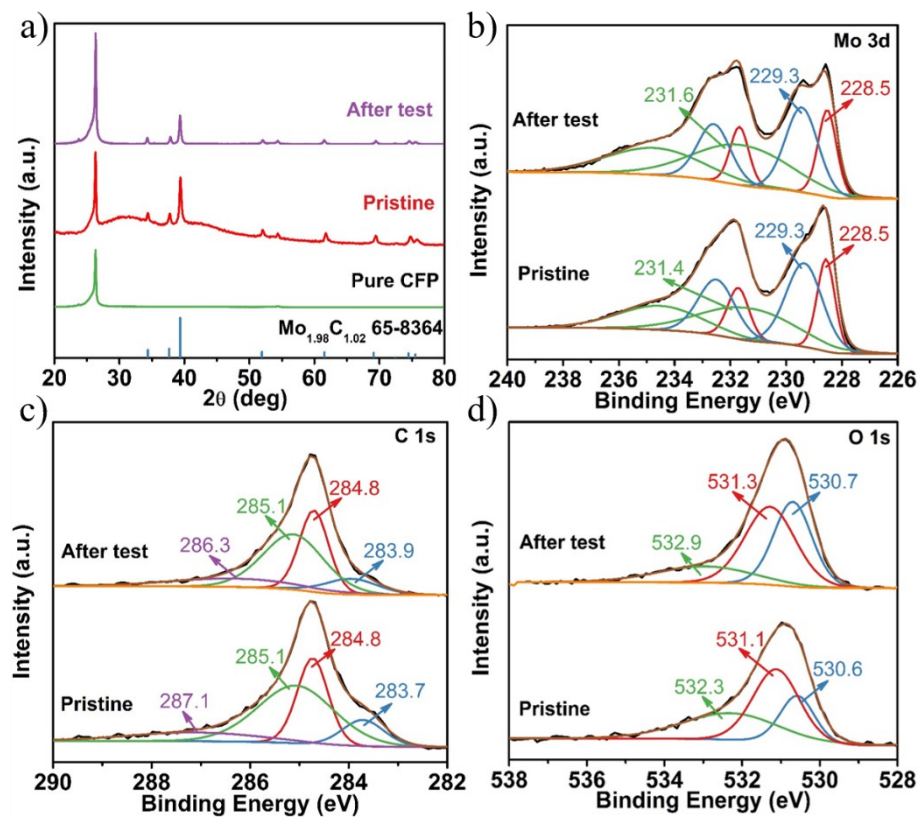


**Figure S8.** (a) XRD pattern, (b) Mo 3d window, (c) C 1s window and (d) O 1a window XPS spectra of the PF- $\text{Mo}_{1.98}\text{C}_{1.02}$  before and after FA decomposition test.

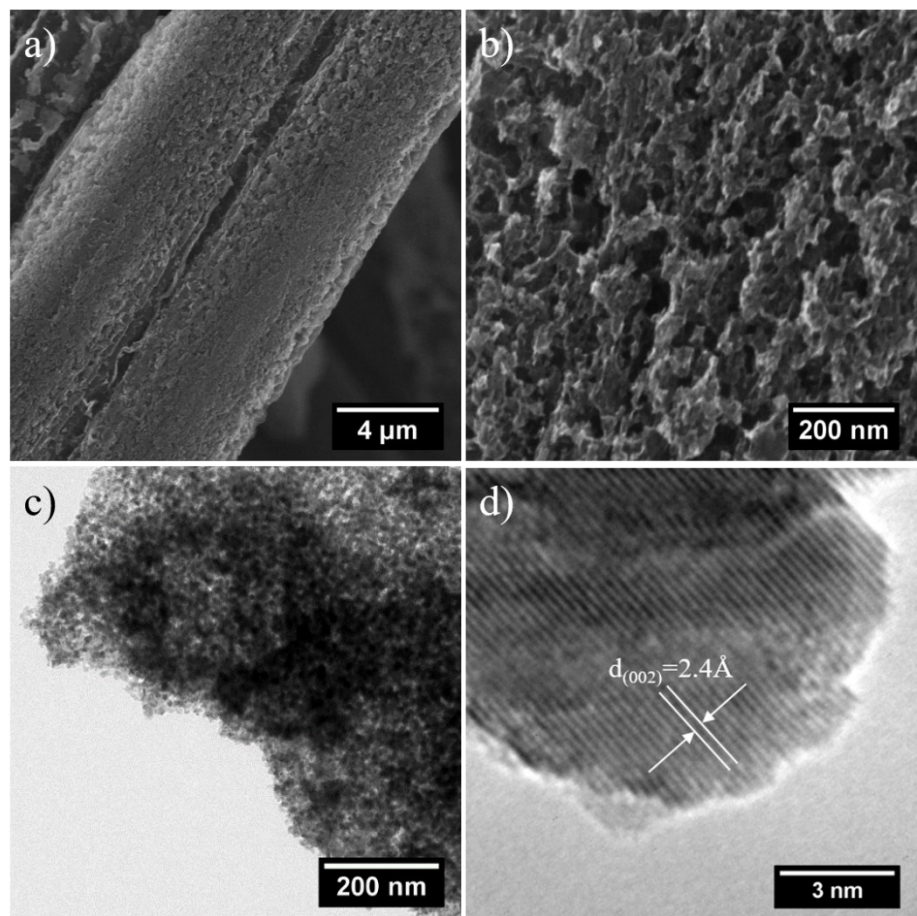


**Figure S9.** (a, b) SEM, (c) TEM, and (d) HRTEM images of the PF- $\text{Mo}_{1.98}\text{C}_{1.02}$  after FA decomposition test.

## DFT calculation:

All calculations were done by means of density functional theory (DFT) as implemented in Vienna ab initio simulation package (VASP).<sup>9</sup> The exchange-correlation term was treated by the generalized gradient approximation (GGA) within the Perdew-Burke-Ernzerhof functional (PBE).<sup>10, 11</sup> The electron ion interaction was described within the projector augmented wave (PAW) pseudopotential.<sup>12</sup> The valence electrons with a plane wave basis up to an energy cutoff of 500 eV was set. A vacuum larger than 15 Å perpendicular to the slab were adopted to avoid the artificial interactions between the slab and its periodic images. During the geometry optimization, all of atoms were allowed to relax by using conjugate-gradient algorithms. Moreover, all geometries were fully optimized to reach the convergence until the Hellman-Feynman force on each ion was smaller than 0.03 eV/Å. The convergence criteria for the electronic structure was set to  $10^{-5}$  eV per atom.

The Gibbs free-energy change ( $\Delta G$ ) of each elementary reaction was calculated as

$$\Delta G = \Delta E + \Delta E_{ZPE} - T\Delta S + \int C_p dT$$

where  $\Delta E$  is the total energy difference directly obtained from DFT calculations. The temperature  $T$  is set to 373.15 K in this work to compare the current DFT results with the experimental data.

$\Delta E_{ZPE}$  is the change in zero-point energies. Moreover, the zero-point energy (ZPE) was calculated from the vibrational frequencies according to

$$E_{ZPE} = \sum_{i=1}^{3N} \frac{\hbar v_i}{2}$$

where  $v_i$  is DFT-calculated normal-mode frequency for species of  $3N$  degree of

freedom (N=number of atoms) adsorbed on Mo<sub>1.98</sub>C<sub>1.02</sub> (002).

$\Delta S$  is the change in entropy. The entropy change of the adsorbed intermediates was calculated from the vibrational frequencies within the harmonic approximation:

$$\Delta S_{ads}(0 \rightarrow T, P^0) = S_{vib} = \sum_{i=1}^{3N} \left[ \frac{\hbar\omega_i}{T(e^{\hbar\omega_i/k_B T} - 1)} - k_B \ln(1 - e^{-\hbar\omega_i/k_B T}) \right]$$

where h is the reduced Planck's constant (1.054573\*10<sup>-34</sup> J S), and k<sub>B</sub> is the Boltzmann constant (1.380649\*10<sup>-23</sup> J K<sup>-1</sup>).

C<sub>P</sub> is the heat capacity at constant volume

$$C_P = \sum_{i=1}^{3N} k_B \left[ \frac{\hbar\omega_i}{k_B T} \right]^2 \frac{e^{\hbar\omega_i/k_B T}}{e^{\hbar\omega_i/k_B T} - 1}$$

The free energies of CO<sub>2</sub> hydrogenation intermediates in reaction pathways were calculated by the computational hydrogen electrode (CHE) model suggested by Nørskov Group.<sup>13-15</sup> By employing the CHE model, a proton/electron (H<sup>+</sup>+e<sup>-</sup>) in solution can be directly treated, and zero voltage is defined based on the reversible hydrogen electrode (RHE), in which the reaction



is defined to be in equilibrium at zero voltage, at all values of pH, at all temperatures, and with H<sub>2</sub> at 101325 Pa pressure.

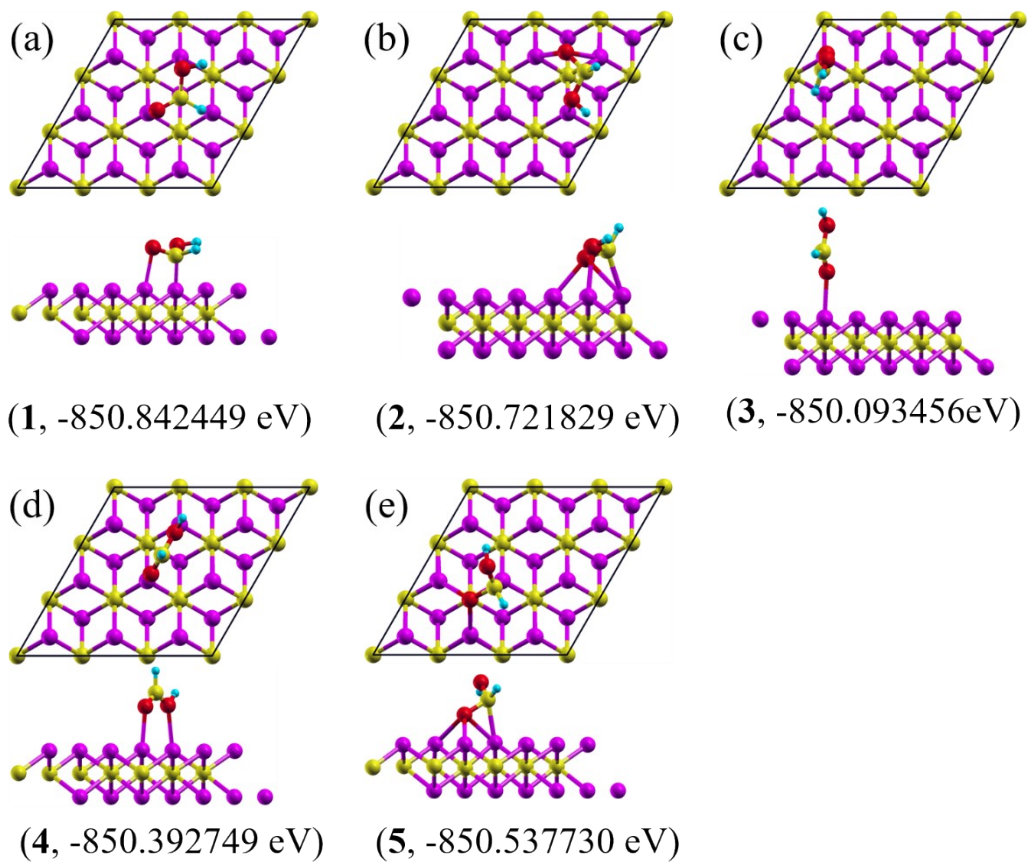


**Figure S10.** Top and side views of the configurations of FA (\*OCHOH) absorbed on the  $\text{Mo}_{1.98}\text{C}_{1.02}(002)$  surface. The configuration 1 exhibits the most stable states with the smallest total energy (E). (●: C; ●: Mo; ●: O; ●: H)

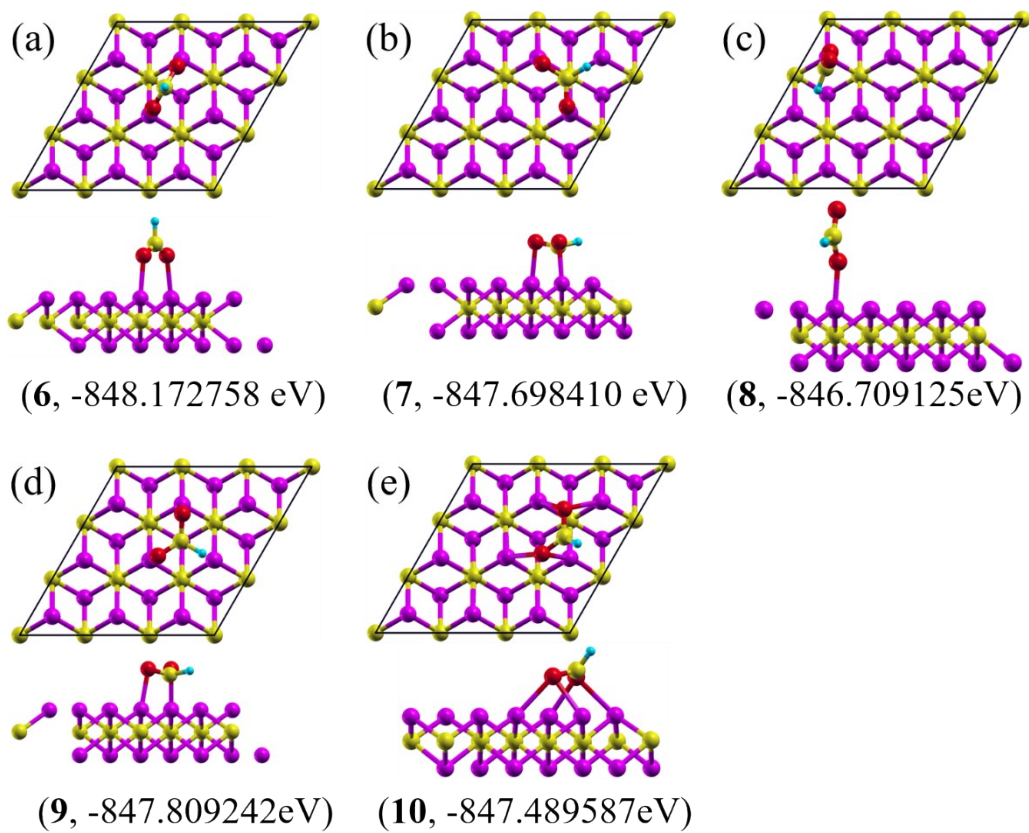


**Figure S11.** Top and side views of the configurations of \*OCHO absorbed on the  $\text{Mo}_{1.98}\text{C}_{1.02}(002)$  surface. The configuration 6 exhibits the most stable states with the smallest total energy (E). (Yellow circle: C; Purple circle: Mo; Red circle: O; Cyan circle: H)

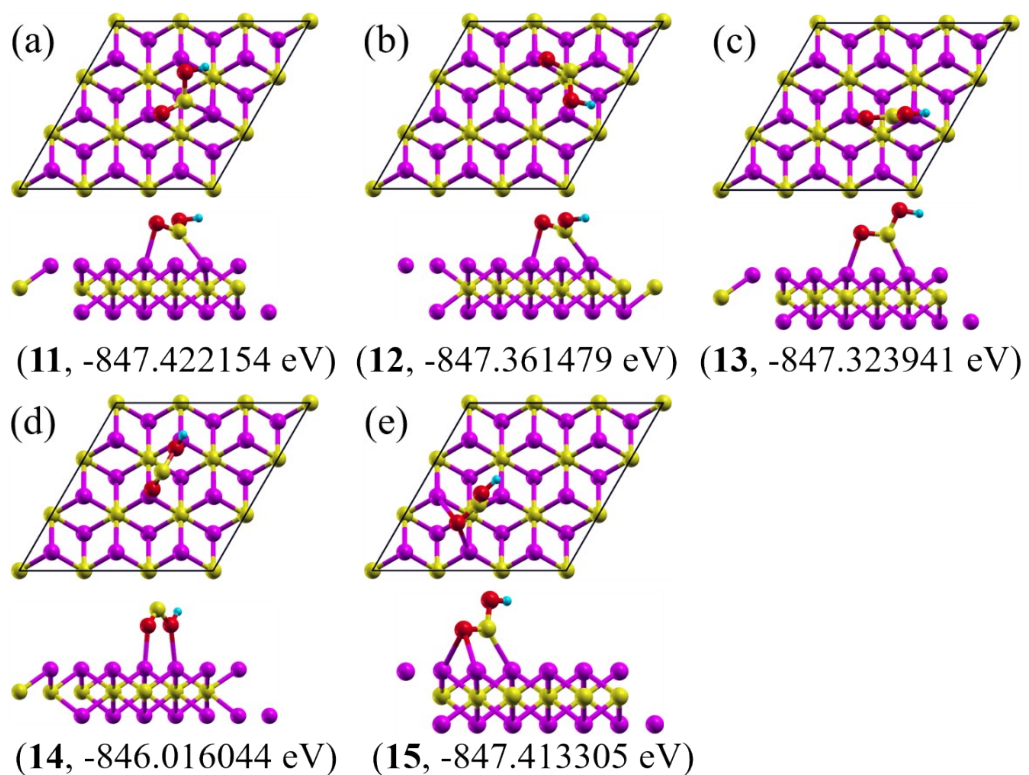


**Figure S12.** Top and side views of the configurations of \*OCOH absorbed on the  $\text{Mo}_{1.98}\text{C}_{1.02}(002)$  surface. The configuration 11 exhibits the most stable states with the smallest total energy (E). (Yellow circle: C; Purple circle: Mo; Red circle: O; Cyan circle: H)

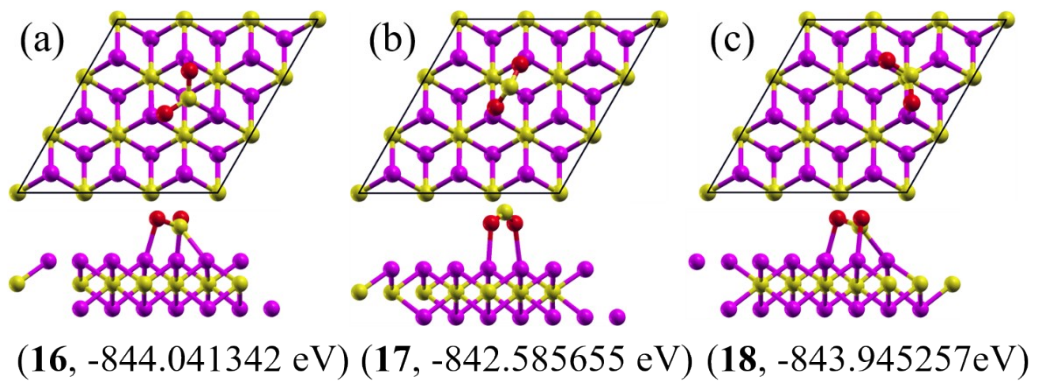


**Figure S13.** Top and side views of the configurations of \*OCO absorbed on the  $\text{Mo}_{1.98}\text{C}_{1.02}(002)$  surface. The configuration 16 exhibits the most stable states with the smallest total energy (E). (●: C; ●: Mo; ●: O; ●: H)

**Table S3.** The adsorption configurations and energies of the FA and the dissociation intermediates on the Mo<sub>1.98</sub>C<sub>1.02</sub>(002) surface.

Dissociation Intermediates	Adsorption Configurations	E	E <sub>ZPE</sub>	-TS	∫C <sub>p</sub> dT
*OCHOH	1	-850.842449	0.852499	0.258988	0.143841
	2	-850.721829	0.898647	0.262738	0.146363
	3	-850.093456	0.924546	0.400739	0.176978
	4	-850.392749	0.919714	0.301921	0.158219
	5	-850.537730	0.888977	0.288488	0.154611
*OCHO	6	-848.172758	0.635713	0.251831	0.130996
	7	-847.698410	0.563737	0.239502	0.128159
	8	-846.709125	0.571859	0.319496	0.137510
	9	-847.809242	0.559186	0.221667	0.122855
	10	-847.489587	0.581280	0.272188	0.138265
*OCOH	11	-847.422154	0.589414	0.238988	0.135060
	12	-847.361479	0.588611	0.241572	0.135839
	13	-847.323941	0.623313	0.279125	0.140444
	14	-846.016044	0.564832	0.308514	0.160344
	15	-847.413305	0.615580	0.271654	0.139172
*OCO	16	-844.041342	0.289747	0.206376	0.115539
	17	-843.945257	0.290805	0.203819	0.115007
	18	-842.585655	0.259356	0.327353	0.151863
*	--	-819.673346	0.000000	0.000000	0.000000
H <sub>2</sub>	--	-6.77008799	0.269128	0.529625	0.112542
CO <sub>2</sub>	--	-22.9539505	0.306855	0.862819	0.128550

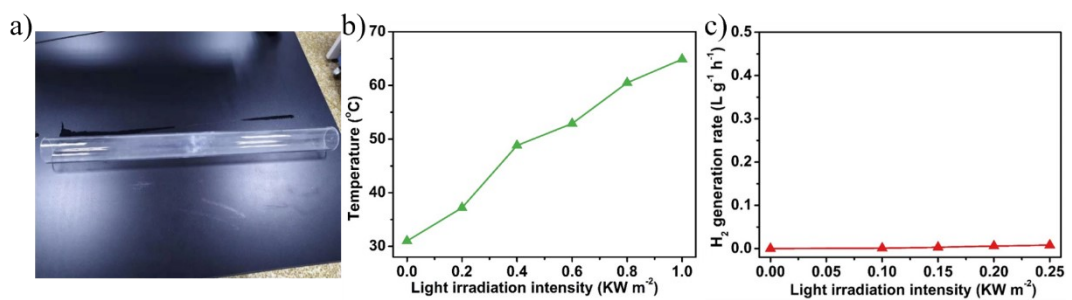


**Figure S14.** (a) Photograph of the general quartz tube. (b) The temperature evolution of the general quartz tube under solar illumination. (c) H<sub>2</sub> generation rate of the PF-Mo<sub>1.98</sub>C<sub>1.02</sub> from FA decomposition over general quartz tube under different intensities of solar irradiation.

**Table S4.** Performances of representative highly efficient non-precious catalysts toward the photocatalytic FA decomposition under sunlight irradiation.

Catalyst	Light	H <sub>2</sub> generation rate (L g <sup>-1</sup> h <sup>-1</sup> )	Reference
TiO <sub>2</sub> nanofibers	AM1.5, 1 sun	0.018	<sup>16</sup>
Cu-TiO <sub>2</sub>	UV	0.019	<sup>17</sup>
Bulk CdS	Visible light, > 400 nm	0.0018	<sup>18</sup>
CdS nanorods	Visible light, > 420 nm	0.0049	<sup>19</sup>
CdS-TNT + WO <sub>3</sub>	Visible light, > 420 nm	0.0139	<sup>20</sup>
CdS@Al-HMS	Visible light, > 420 nm	0.0029	<sup>21</sup>
CdS/ZnS nanoparticles	Visible light, > 420 nm	0.0278	<sup>22</sup>
Ni <sub>2</sub> P/Zn <sub>3</sub> In <sub>2</sub> S <sub>6</sub>	Visible light, > 400 nm	0.0102	<sup>23</sup>
MoP/Zn <sub>3</sub> In <sub>2</sub> S <sub>6</sub>	Visible light, > 400 nm	0.0208	<sup>23</sup>
Cu <sub>3</sub> P/Zn <sub>3</sub> In <sub>2</sub> S <sub>6</sub>	Visible light, > 400 nm	0.0013	<sup>23</sup>
CoP/Zn <sub>3</sub> In <sub>2</sub> S <sub>6</sub>	Visible light, > 400 nm	0.0017	<sup>23</sup>
WP <sub>2</sub> /Zn <sub>3</sub> In <sub>2</sub> S <sub>6</sub>	Visible light, > 400 nm	0.0011	<sup>23</sup>
MoS <sub>2</sub> /Zn <sub>3</sub> In <sub>2</sub> S <sub>6</sub>	Visible light, > 420 nm	0.0166	<sup>24</sup>
CdS@ZIF-8	Visible light, > 420 nm	0.02016	<sup>25</sup>
PF-Mo <sub>1.98</sub> C <sub>1.02</sub>	AM1.5, 0.25 sun	1.07	This work

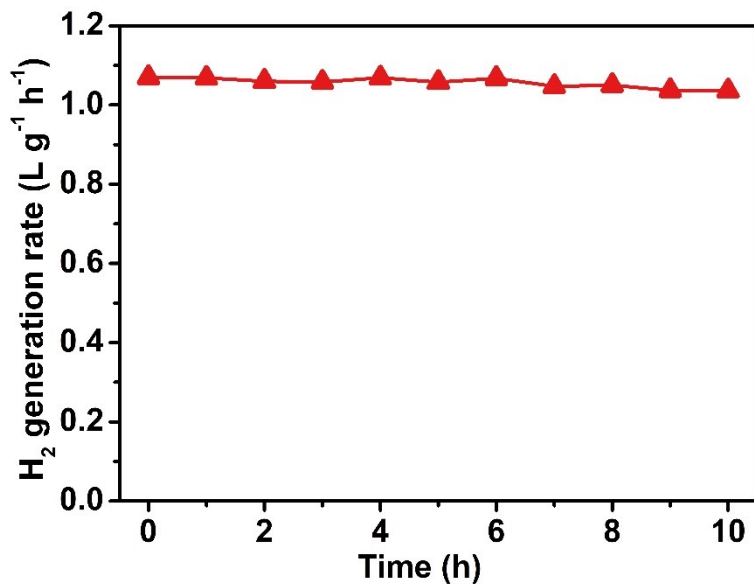


**Figure S15.** FA decomposition stability of  $\text{PF-Mo}_{1.98}\text{C}_{1.02}$  under the solar illumination of  $0.25 \text{ KW m}^{-2}$ .

## References

1. C. Ding, T. Shen, Y. Yang and X. Xu, *ACS Catal.*, 2020, **10**, 5153-5162.
2. A. k. Koo's and F. Solymosi, *Catal. Lett.*, 2010, **138**, 23-27.
3. D. H. Carrales-Alvarado, A. B. Dongil, J. M. Fernández-Morales, M. Fernández-García, A. Guerrero-Ruiz and I. Rodríguez-Ramos, *Catal. Sci. Technol.*, 2020, **10**, 6790-6799.
4. J. T. Gray, S. W. Kang, J.-I. Yang, N. Kruse, J.-S. McEwen, J. C. Park and S. Ha, *Appl. Catal. B: Environ.*, 2020, **264**, 118478.
5. V. O. Koroteev, D. A. Bulushev, A. L. Chuvilin, A. V. Okotrub and L. G. Bulusheva, *ACS Catal.*, 2014, **4**, 3950-3956.
6. J. Wang, J. Cao, Y. Ma, X. Li, P. Xiaokaiti, X. Hao, T. Yu, A. Abudula and G. Guan, *Energy Convers. Manage.*, 2017, **147**, 166-173.
7. J. Cao, J. Wang, Y. Ma, X. Li, P. Xiaokaiti, X. Hao, A. Abudula and G. Guan, *J. Alloy. Compd.*, 2018, **735**, 1463-1471.
8. S. Zhu, Z. Pan, Y. Tao and Y. Chen, *J. Renew. Mater.*, 2020, **8**, 939-946.
9. G. Kresse, *J. Non-Cryst. Solids*, 1995, **192**, 222-229.
10. J. P. Perdew, K. Burke and M. Ernzerhof, *Phys. Rev. Lett.*, 1996, **77**, 3865.
11. J. P. Perdew, K. Burke and M. Ernzerhof, *Phys. Rev. Lett.*, 1997, **78**, 1396.
12. P. E. Blöchl, *Phys. Rev. B*, 1994, **50**, 17953.
13. Z. W. Seh, J. Kibsgaard, C. F. Dickens, I. Chorkendorff, J. K. Nørskov and T. F. Jaramillo, *Science*, 2017, **355**, 146.
14. D. M. Koshy, S. S. Nathan, A. S. Asundi, A. M. Abdellah, S. M. Dull, D. A. Cullen, D. Higgins, Z. Bao, S. F. Bent and T. F. Jaramillo, *Angew. Chem. Int. Ed.*,

2021, **60**, 2-11.

15. L. Wang, H. Peng, S. Lamaison, Z. Qi, D. M. Koshy, M. B. Stevens, D. Wakerley, J. A. Z. Zeledo' n, L. A. King, L. Zhou, Y. Lai, M. Fontecave, J. Gregoire, F. Abild-Pedersen, T. F. Jaramillo and C. Hahn, *Chem. Catal.*, 2021, DOI:<https://doi.org/10.1016/j.chechat.2021.05.006>.
16. Z. Zhang, S. Cao, Y. Liao and C. Xue, *Appl. Catal. B: Environ.*, 2015, **162**, 204-209.
17. V. Lanese, D. Spasiano, R. Marotta, I. Di Somma, L. Lisi, S. Cimino and R. Andreozzi, *Int. J. Hydrogen Energy*, 2013, **38**, 9644-9654.
18. I. Willner and Z. Goren, *J. Chem. Soc. Chem. Commun.*, 1986, 172-173.
19. Y. Li, Y. Hu, S. Peng, G. Lu and S. Li, *J. Phys. Chem. C*, 2009, **113**, 9352-9358.
20. H. M. Yeh, S. L. Lo, M. J. Chen and H. Y. Chen, *Water Sci. Technol.*, 2014, **69**, 1676-1681.
21. Y. Zhang, L. Zhang and S. Li, *Int. J. Hydrogen Energy*, 2010, **35**, 438-444.
22. X. Wang and X. Li, *Mater. Sci. Eng. B*, 2014, **181**, 86-92.
23. S. Duan, S. Zhang, S. Chang, S. Meng, Y. Fan, X. Zheng and S. Chen, *Int. J. Hydrogen Energy*, 2019, **44**, 21803-21820.
24. S. Zhang, S. Duan, G. Chen, S. Meng, X. Zheng, Y. Fan, X. Fu and S. Chen, *Chinese J. Catal.*, 2021, **42**, 193-204.
25. M. Zeng, Z. Chai, X. Deng, Q. Li, S. Feng, J. Wang and D. Xu, *Nano Research*, 2016, **9**, 2729-2734.